Stable single-mode operation of surface-emitting terahertz lasers with graded photonic heterostructure resonators

Gangyi Xu, Yacine Halioua, Souad Moumdji, Raffaele Colombelli, Harvey E. Beere et al.

Additional information on Appl. Phys. Lett.
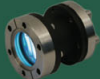
Stable single-mode operation of surface-emitting terahertz lasers with graded photonic heterostructure resonators

Gangyi Xu,[1] Yacine Halioua,[1] Souad Moumdji,[1] Raffaele Colombelli,[1] Harvey E. Beere,[2] and David A. Ritchie[2]

[1]*Institut d'Electronique Fondamentale, Univ. Paris Sud, UMR8622 CNRS, 91405 Orsay, France*
[2]*Cavendish Laboratory, University of Cambridge, Cambridge CB3 0HE, United Kingdom*

Graded photonic heterostructures (GPH) can be regarded as energy wells for photons. We show that judicious engineering of such photonic wells, obtained by tailoring the grading and the slit width of the GPH resonator, allows one to ensure spectrally single-mode emission on the fundamental symmetric mode in the whole lasing dynamical range of terahertz quantum cascade lasers. Furthermore, the radiative character of the symmetric mode leads to single-mode emission with mW output power in continuous-wave operation, as well as to single-lobed far-field beam patterns. A careful combination of theoretical analysis and experimental observations reveals that the results stem from interplay between mode competition and spatial hole burning effects. © 2013 AIP Publishing LLC. [http://dx.doi.org/10.1063/1.4809918]

Terahertz quantum cascade lasers[1] (THz QCLs) with stable single-mode emission and sufficient output power are of high importance for the applications related, for instance, to trace-gas detection.[2,3] Although second-order distributed feedback (DFB)[4–8] and 2D photonic crystal[9–15] THz QCLs, based on metal-metal waveguides and perfectly periodic lattices, have exhibited single-mode emission, they suffer from low power efficiency because of the anti-symmetric character of the laser modes.[9,14] Several strategies such as second-order DFB lasers with dual-slits and third-order DFB lasers[16–19] have been proposed to improve the power efficiency, as well as the beam directionality.

We have recently demonstrated surface-emitting THz QCLs based on graded photonic heterostructure (GPH) resonators,[20] as shown schematically in Figs. 1(a) and 1(b). The GPH resonator acts as an energy well for photons: the symmetric modes are spatially confined in the center of the grating, while the anti-symmetric ones are relegated towards the highly lossy edges where the absorbing boundaries located. Judiciously designed GPH resonators force the laser to operate on the fundamental symmetric mode with significantly increased radiation loss. As a result, GPH lasers with resonant-phonon active region have exhibited stable single-mode emission with very high power efficiency in pulsed mode, as well as low-divergence single-lobed emission patterns.[20]

In the subsequent research activity aiming at achieving continuous-wave (cw) operation of GPH lasers by exploiting bound-to-continuum active regions, the excitation of other modes has been observed at high injection levels. The possible reasons are the large relative dynamical range related to the bound-to-continuum active regions and the broadened gain spectrum caused by the thick active region experimentally used, which provides sufficient gain to other modes. It is thus important to understand the mode competition in GPH lasers and to develop an effective solution to obtain stable single-mode emission within a large dynamical range.

The GPH resonator can be understood by considering three modes: the first symmetric (S1) mode, the second symmetric (S2) mode, and the first antisymmetric (A1) mode. These modes are close in frequency, i.e., their separation is usually less than the gain width of the laser active region. The material losses (α_{mat}) of the three modes are also similar, ≈ 20–$30\,\mathrm{cm}^{-1}$, calculated with a 1D simulation of the mode profile and the effective refractive index. The complex refractive index of the metal, the highly doped contact layers, and the active region are obtained in the framework of a Drude model.[21,22] What discriminate them are the cavity losses α_{cav}, which consist of radiation loss α_{rad} caused by light radiated from the laser surface and the in-plane loss $\alpha_{in\text{-}plane}$ due to the light leaked *in-plane* out of the cavity, $\alpha_{cav} = \alpha_{rad} + \alpha_{in\text{-}plane}$. They are highly dependent on the GPH structure and affect important laser parameters such as the threshold current density, the power slope efficiency, and the dynamical range.

In this letter we elucidate the competition mechanisms between these three modes and their dependence on the *photonic potential* induced by the GPH structure. Judicious engineering of the height of the photonic barrier and of the slit widths enables laser operation on the fundamental symmetric mode in almost the whole dynamical range, with high slope efficiency, and low threshold current densities. CW operation is systematically achieved, with $\approx 4\,\mathrm{mW}$ power at 15 K and 0.3% wall-plug efficiency (WPE).

We have employed a QCL structure (wafer V414) based on a bound-to-continuum active region.[23] Because of its low parasitic current, the loss of each mode can be better reflected on the threshold current density.[13] The reduced applied bias and the lower threshold current density, compared to phonon-resonant active regions, contribute to realize the cw operation of GPH lasers. The QCL core consists of 90 repetitions of the active region, for a total thickness of $\approx 12\,\mu\mathrm{m}$, and a designed emission frequency of $\approx 2.7\,\mathrm{THz}$. The GPH structures (metallic gratings), which also act as the top electrode, were defined on the top of the active core by
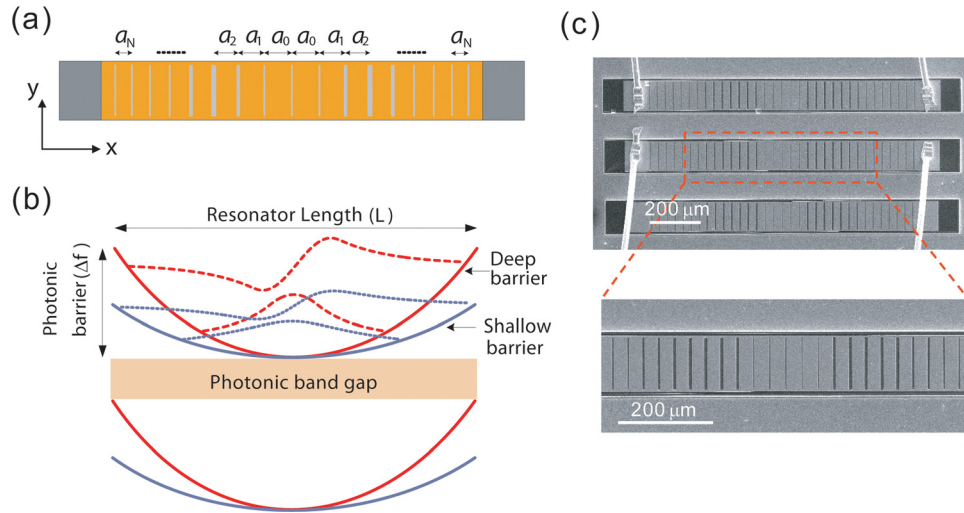
FIG. 1. (a) Schematic top view of a surface-emitting THz QCL with a GPH resonator. The lattice spacing (a_i) of the top metallic grating is symmetrically and gradually decreased from the centre toward each end of the laser ridge, according to the rule: $a_{i+1} = a_i - \Delta a$ ($i = 0, 1, 2, \ldots$), where a_i is the periodicity of the i-th slit from the center, and Δa is a constant. (b) Schematic real-space photonic band diagram of the GPH resonator. The height of the photonic barrier Δf is defined as the frequency difference between the photonic band edge of a periodic grating with lattice constant a_0 and the one with the lattice constant being a_N. The solid gray (red) curves correspond to the band edges of a GPH structure with a shallow (deep) photonic barrier. The field envelopes of the confined symmetric modes S1 and S2 are also shown in a shallow photonic barrier (dashed gray curves) and in a deep barrier (dashed red curves), respectively. (c) A SEM image of typical GPH lasers with an expanded view of the GPH resonator.

contact optical lithography followed by metal deposition (Ti/Au, 10/500 nm) and lift-off. The top doped GaAs contact layer was left in place at each end of the ridges and also along the sides of the grating to provide absorbing boundary conditions. More details on material growth and device fabrication can be found in Refs. 20 and 24. Figure 1(c) shows a scanning electron microscope (SEM) image of typical GPH lasers with an expanded view of the GPH resonator.

We implemented two different generations of GPH lasers. The first generation is designed to endow the mode S1 with low total loss and an extended field envelope. This configuration should lead to a laser with low threshold current density and large lasing dynamical range since an extended field envelope maximizes its overlap with the gain region along the laser ridge. To extend the field envelope, we have fabricated a long GPH resonator with a shallow photonic well: the resonator consists of 39 periods with a small periodicity grading ($\Delta a = a_i - a_{i+1} = 0.1 \, \mu m$, where a_i is the periodicity of the i-th slit. The resulting photonic barrier height is $\Delta f = 0.1$ THz (or $\sim 3.3 \, cm^{-1}$ in wavenumbers), approximately half of the photonic bandgap of the constituent grating with uniform periodicity a_i (typically about 0.25 THz). The definition of Δf is given in the caption of Fig. 1(b). Narrow slits ($\sim 1.5 \, \mu m$ wide) are necessary to ensure a low cavity loss α_{cav} for the S1 mode, because its α_{cav} is dominated by the radiation loss α_{rad} and it is proportional to the effective area of the slits.

Finite-difference time-domain (FDTD) simulations show that the normalized wavelength (a_0/λ) is 0.306, 0.310, and 0.288 for the modes S1, S2, and A1, respectively. Here, λ is the wavelength in vacuum and a_0 is the periodicity of the slit at the center of the GPH structure. The corresponding cavity losses α_{cav} are 8.3, 11.3, and 16.8 cm^{-1}, respectively. Figs. 2(a)–2(c) (black lines with square symbols) present the normalized intensity envelope of each mode. The simulations illustrate that modes S1 and S2 are both well confined

inside the resonator; therefore, their cavity losses are dominated by the radiation loss α_{rad}. In contrast, the antisymmetric mode A1 is pushed close to the ends of the resonator with a considerable part of light leaking into the highly lossy edges, resulting in a high $\alpha_{in\text{-}plane}$ which determines the total cavity loss. The simulations indicate that the GPH laser will operate on the mode S1 for its lowest total loss. However, we should keep in mind the weak relative contrast of the
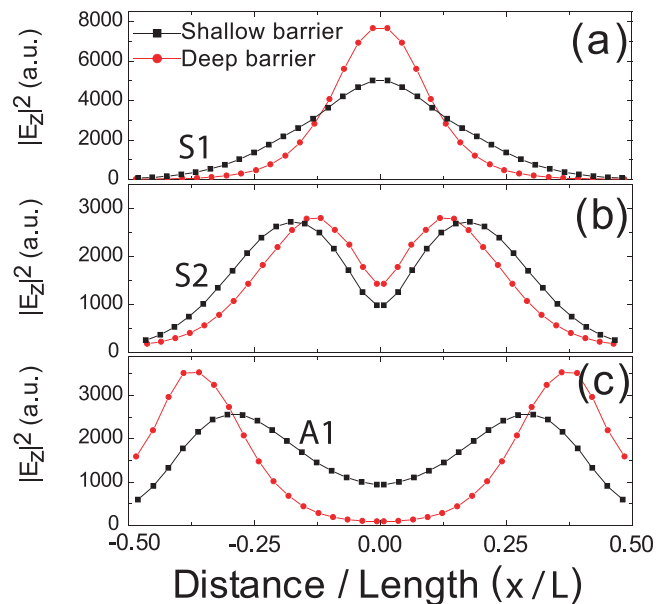

FIG. 2. Normalized intensity distributions ($|E_z|^2 / \int_{-L/2}^{L/2} |E_z|^2 dx$) along the laser ridge for the modes S1 (a), S2 (b), and A1 (c), calculated by FDTD simulations. E_z is the vertical component (perpendicular to the quantum well plane) of the electric field, and L the length of the GPH resonator. The highly lossy edges are approximated by the perfectly matched layers in the simulations. The black curves with square symbols correspond to the first generation GPH resonator with a shallow photonic barrier. The red curves with circular symbols correspond to the second generation GPH resonator with a deep photonic barrier.
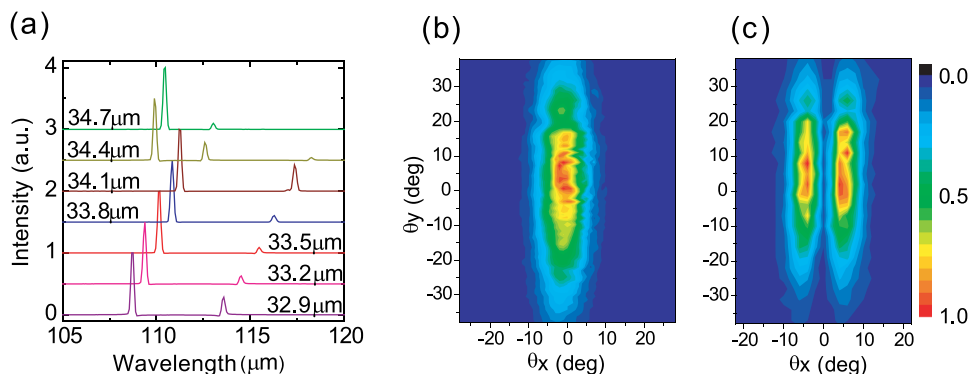
FIG. 3. Spectral and far-field characteristics of the first generation GPH lasers with shallow photonic barriers. (a) Normalized emission spectra of lasers with different a_0, as marked in the figure. For clarity, each spectrum is shifted in the vertical direction according to the value of a_0. (b) Far-field beam pattern of a GPH laser ($a_0 = 33.8\,\mu m$, ridge width 127 μm) measured at about $1.1 \times J_{th}$, at low temperature (15 K), where only the mode $a_0/\lambda = 0.305$ exists. (c) Far-field beam pattern of a GPH laser ($a_0 = 34.7\,\mu m$, ridge width 157 μm) measured at about $2.0 \times J_{th}$, at low temperature (15 K), where the intensity of the mode $a_0/\lambda = 0.313$ is more than one order of magnitude higher than the other two modes. θ_x and θ_y are angular directions along and perpendicular to the laser ridge, respectively, and the $\theta_x = \theta_y = 0$ angle corresponds to the direction orthogonal to the device surface.

total loss α_{total} ($\alpha_{total} = \alpha_{mat} + \alpha_{cav}$) among the three modes and the fact that the intensity of each mode peaks at different parts of the laser ridge.

Figure 3(a) shows the lasing spectra of the GPH lasers with shallow photonic barriers. Several devices with different a_0 are measured at ≈ 1.5 times the threshold current density (J_{th}). The figure highlights the onset of three modes whose wavelengths scale linearly with the photonic lattice periodicity a_0. Their normalized wavelengths (a_0/λ) are 0.305, 0.313, and 0.290, respectively, in good agreement with the calculated values of the modes S1, S2, and A1. To further corroborate the mode identification, we measured the far-field emission pattern of the two symmetric modes. We have selected two lasers with different a_0 (33.8 and 34.7 μm) where the modes $a_0/\lambda = 0.305$ (S1) and 0.313 (S2) are located near the peak gain. Judiciously choosing the injection current allows one to operate the lasers almost exclusively on one mode. The resulting far-field patterns are reported in Figs. 3(b) and 3(c). The mode with $a_0/\lambda = 0.305$ exhibits a single-lobed beam pattern with maximum emission orthogonal to the laser surface. The mode with higher frequency ($a_0/\lambda = 0.313$) exhibits instead a two-lobed beam pattern with a central nodal line. The combination of mode frequency and far-field beam patterns unequivocally confirms that the emission at $a_0/\lambda = 0.305$ and 0.313 stems from the modes S1 and S2, respectively.

The light-voltage-current density (L-V-J) characteristics measured in cw for a first generation GPH laser with $a_0 = 33.8\,\mu m$ are reported in Fig. 4(a) (black curves with square symbols). This device is chosen since the frequency of the S1 mode is close to the peak gain. Figure 4(b) shows the emission spectra of the laser at different injected currents. At threshold the laser operates only on the mode S1: it is the mode with lowest total loss α_{total}. The A1 mode appears at about $1.3 \times J_{th}$, and the onset of mode S2 occurs close to J_{max} ($\sim 2.0 \times J_{th}$). The appearance of the other two modes stems from spatial hole burning effects: as shown in Fig. 2 their electromagnetic intensity peaks at different regions of the laser ridge.

Note that although the calculated α_{cav} of mode A1 is higher than that of mode S2, the former one reaches laser threshold earlier than the latter one. It is again due to spatial

hole-burning effects: the overlap of the field envelopes between S1 and A1 is very limited. These results indicate the strategy to achieve stable single mode emission in the whole dynamical range: increasing the cavity loss (α_{cav}) difference between S1 and the other two modes to overcome the spatial hole-burning effects.

The second generation of GPH lasers (fabricated from the same wafer V414) aims exactly at that. We have implemented a deep photonic barrier ($\Delta f = 0.3$ THz, or $\sim 10\,cm^{-1}$ in wavenumbers), and the effects on the photonic envelope functions ($|E_z|^2$) are reported in Fig. 2 (red curves with circular symbols). The A1 mode is further pushed toward the absorbing boundaries, thus increasing its α_{cav} value. At the same time, the confinement of modes S1 and S2 are both enhanced. To further enlarge the difference of α_{cav} between modes S1 and S2, we increase the slit width where the intensity of mode S2 reaches its maxima as shown in Fig. 1(c). It is because again, for the confined symmetric modes, the dominant radiation loss is proportional to the effective emission area of the related mode. The second generation GPH resonators feature α_{cav} values of 11.6, 19.7, and 133 cm^{-1} for the modes S1, S2, and A1, respectively. In particular, mode A1 sees its α_{cav} value dramatically increased with respect to the first generation (from 16.8 to 133 cm^{-1}).

Figure 4(a) (red line with circular symbols) shows the cw L-V-J curves for a typical second generation GPH laser ($a_0 = 33.8\,\mu m$). Figure 4(c) shows the corresponding laser emission spectra at different injection currents, which demonstrate that single mode emission is achieved in the whole lasing dynamical range. Figure 4(d) presents the far-field beam pattern of the second generation laser at a temperature of 15 K. The normalized wavelength and the far-field beam pattern confirm that the mode S1 is the active one. We have also realized on-chip lithographic frequency tuning of the second generation GPH lasers. The emission wavelength scales approximately linearly from $\lambda = 106.7\,\mu m$ to $\lambda = 111.8\,\mu m$ when the lattice parameter (a_0) changes from 33.2 to 34.7 μm. A larger tuning range can be obtained, since it is only limited by the gain bandwidth of the active region. Figure 4(a) also shows that by using a deep photonic barrier J_{th} increases from 100 A/cm^2 to 110 A/cm^2, and the power slope efficiency near the threshold increases from 48 to 70 mW/(kA cm^{-2}). The variations of J_{th} and power
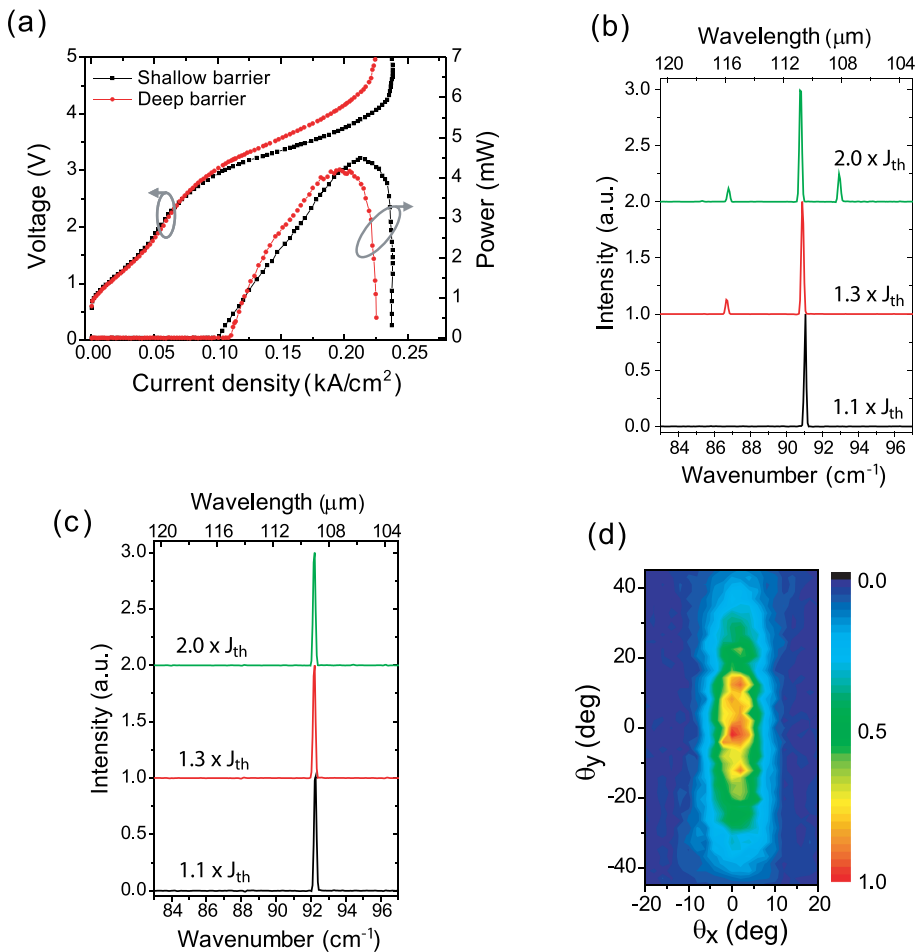
FIG. 4. (a) Light-voltage-current density (*L-V-J*) curves of two GPH lasers measured in cw mode at 15 K. The black curves with square symbols correspond to the first generation laser ($a_0 = 33.8 \, \mu$m) with a shallow photonic barrier, while the red curves with circular symbols correspond to the second generation laser ($a_0 = 33.8 \, \mu$m) with a deep barrier. Panels (b) and (c) are the corresponding emission spectra of the first and the second generation GPH lasers, respectively, measured at different injected currents. Panel (d) presents the far-field emission pattern of the second generation laser measured at a temperature of 15 K.

efficiency reflect well the higher radiation loss of the second generation GPH lasers. Note that the two lasers exhibit similar slope efficiencies in the current density range between 0.14 and 0.18 kA/cm^2. This might be due to the electric-field-dependence of the gain spectrum and also due to the onset of the other two modes in the shallow barrier device.

Above laser threshold, the differential resistance ($\partial V/\partial J$) of the deep photonic barrier laser ($1.05 \times 10^{-2} \, \Omega \, \text{cm}^2$) is higher than the shallow barrier laser ($7.2 \times 10^{-3} \, \Omega \, \text{cm}^2$), resulting in a narrower dynamical range. As a matter of fact, in the lasing regime the current linked to photon-assisted tunneling cannot be neglected (elevated photon density in the cavity). In the laser with shallow photonic barrier, photon-driven electronic transport takes place in the whole resonator volume because of the extended field envelope of mode S1 and also because mode A1 is active. Conversely, in the laser with deep photonic barrier the photon-driven transport is dominant only in the central part of the resonator. This is possibly the main reason behind the higher differential resistance above threshold and the narrower dynamical range observed in the deep barrier laser. The maximum cw output powers of two lasers are respectively 4.5 mW and 4.2 mW at 15 K, measured with a high sensitivity thermal power meter (OPHIR 3A-P-THz), and the corresponding wall-plug efficiencies are about 0.3%.

In conclusion, we have demonstrated the design flexibility of resonators based on the graded photonic heterostructure concept. Judicious engineering of the photonic wavefunctions of symmetric and antisymmetric modes allows one to perform a global laser device optimization, at least in the case of THz QCLs. We have demonstrated stable spectrally single-mode emission on the fundamental, radiative, symmetric mode in the whole dynamical range, with mW-range output power in cw operation, and elevated power efficiencies. The next step will be the extension of this powerful concept to 2D devices.

[1]R. Köhler, A. Tredicucci, F. Beltram, H. Beere, E. H. Linfield, A. G. Davies, D. A. Ritchie, R. C. Iotti, and F. Rossi, Nature (London) **417**, 156 (2002).
[2]M. Tonouchi, Nat. Photonics **1**, 97 (2007).
[3]B. S. Williams, Nat. Photonics **1**, 517 (2007).
[4]J. A. Fan, M. A. Belkin, F. Capasso, S. Khanna, M. Lachab, A. G. Davies, and E. H. Linfield, Opt. Express **14**, 11672–11680 (2006).
[5]S. Kumar, B. S. Williams, Q. Qin, A. W. M. Lee, and Q. Hu, Opt. Express **15**, 113–128 (2007).
[6]L. Mahler, A. Tredicucci, F. Beltram, C. Walther, H. E. Beere, and D. A. Ritchie, Opt. Express **17**, 6703 (2009).
[7]L. Mahler, A. Tredicucci, F. Beltram, C. Walther, J. Faist, B. Witzigmann, H. E. Beere, and D. A. Ritchie, Nat. Photonics **3**, 46 (2009).
[8]E. Mujagic, C. Deutsch, H. Detz, P. Klang, M. Nobile, A. M. Andrews, W. Schrenk, K. Unterrainer, and G. Strasser, Appl. Phys. Lett. **95**, 011120 (2009).
[9]Y. Chassagneux, R. Colombelli, W. Maineult, S. Barbieri, H. Beere, D. Ritchie, S. P. Khanna, E. H. Linfield, and A. G. Davies, Nature (London) **457**, 174–178 (2009).

[10]H. Zhang, G. Scalari, J. Faist, L. A. Dunbar, and R. Houdre, J. Appl. Phys. **108**, 093104 (2010).

[11]L. Sirigu, R. Terazzi, M. I. Amanti, M. Giovannini, J. Faist, L. A. Dunbar, and R. Houdré, Opt. Express **16**, 5206 (2008).

[12]Y. Chassagneux, R. Colombelli, W. Maineult, S. Barbieri, S. P. Khanna, E. H. Linfield, and A. G. Davies, Appl. Phys. Lett. **96**, 031104 (2010).

[13]Y. Chassagneux, Q. J. Wang, S. P. Khanna, E. Strupiechonski, J.-R. Coudevylle, E. H. Linfield, A. G. Davies, F. Capasso, M. Belkin, and R. Colombelli, IEEE Trans. Sci. Technol. **2**, 83 (2012).

[14]G. Sevin, D. Fowler, G. Xu, F. H. Julien, R. Colombelli, S. P. Khanna, E. H. Linfield, and A. G. Davies, Appl. Phys. Lett. **97**, 131101 (2010).

[15]A. Benz, Ch. Deutsch, G. Fasching, K. Unterrainer, A. M. Andrews, P. Klang, W. Schrenk, and G. Strasser, Opt. Express **17**, 941 (2009).

[16]L. Mahler, A. Tredicucci, F. Beltram, C. Walther, J. Faist, H. E. Beere, and D. A. Ritchie, Appl. Phys. Lett. **96**, 191109 (2010).

[17]M. I. Amanti, M. Fischer, G. Scalari, M. Beck, and J. Faist, Nat. Photonics **3**, 586 (2009).

[18]M. I. Amanti, G. Scalari, F. Castellano, M. Beck, and J. Faist, Opt. Express **18**, 6390 (2010).

[19]T.-Y. Kao, Q. Hu, and J. L. Reno, Opt. Lett. **37**, 2070 (2012).

[20]G. Xu, R. Colombelli, S. P. Khanna, A. Belarouci, X. Letartre, L. Li, E. H. Linfield, A. G. Davies, H. E. Beere, and D. A. Ritchie, Nat. Commun. **3**, 952 (2012).

[21]B. S. Williams, S. Kumar, H. Callebaut, Q. Hu, and J. L. Reno, Appl. Phys. Lett. **83**, 2124 (2003).

[22]S. Fathololoumi, E. Dupont, Z. R. Wasilewski, C. W. I. Chan, S. G. Razavipour, S. R. Laframboise, S. Huang, Q. Hu, D. Ban, and H. C. Liu, J. Appl. Phys. **113**, 113109 (2013).

[23]G. Sevin, D. Fowler, G. Xu, F. H. Julien, R. Colombelli, H. Beere, and D. Ritchie, Electron. Lett. **46**, 1513 (2010).

[24]E. Strupiechonski, D. Grassani, D. Fowler, F. H. Julien, S. P. Khanna, L. Li, E. H. Linfield, A. G. Davies, A. B. Krysa, and R. Colombelli, Appl. Phys. Lett. **98**, 101101 (2011).